Dendritic Growth and Morphology Selection in Copper Electrodeposition from Acidic Sulfate Solutions Containing Chlorides

Wenbo Shao and Giovanni Zangari*

The Department of Materials Science and Engineering and Center for Electrochemical Science and Engineering, University of Virginia, 116 Engineers Way, Charlottesville, Virginia 22904-4745

We investigate the morphology of Cu films electrodeposited onto silicon from an acidic sulfate electrolyte with the addition of a variable concentration of chloride anions. Addition of chloride increases grain size and the degree of grain faceting while decreasing the density of growth nuclei. Well-developed monocrystalline dendrites are formed in acidic sulfate solutions with high concentration of chloride. Dendrites form under growth conditions that either approach diffusion limitation, or occur within a potential range where different crystallographic faces exhibit a different potential dependence for chloride desorption. The presence of dendrites however is mainly related to the fact that the reduction route $Cu^{2+} \rightarrow CuCl \rightarrow Cu$ becomes the rate-determining process in solutions with high chloride concentration; the rate of this reaction is largest at {110} planes, where the concentration of chloride anions is the highest, generating dendrites with branches along the {110} directions.

Introduction

The morphology of electrodeposited metals is determined by the interplay of various atomistic phenomena occurring in electrocrystallization, in particular the transport of ions toward the electrode and the dynamics of surface processes.[1,2] The establishment of a correlation between these phenomena and the formation of morphology is important in order to control film microstructure by monitoring the deposition parameters. In particular, in practical applications dendritic growth should be best avoided when dense and compact films are sought;[3–6] on the other hand, it may be required in cases where formation of materials with high surface areas is pursued.[7]

Copper is a good model system for the investigation of this correlation since the kinetics and reaction mechanism of copper reduction are well-known. For instance, copper electrodeposition from acidic cupric sulfate solutions is known to occur through two successive one-electron transfer reactions

$$Cu^{2+} + e^- = Cu^+ \qquad E^0 = -0.087 \text{ V}_{SCE} \qquad (1)$$

$$Cu^+ + e^- = Cu \qquad E^0 = 0.281 \text{ V}_{SCE} \qquad (2)$$
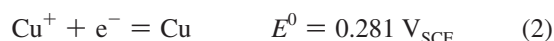
of which the former is the rate-determining step (RDS).[8–10]

However, copper reduction can also proceed along an alternative path when chloride ions are present in solution, through the formation at the electrode surface of a CuCl monolayer, generated by the following reaction[11]

$$Cu^2 + Cl^-_{ads} + e^- = CuCl_{ads} \qquad E^0 = 0.338 \text{ V}_{SCE} \qquad (3)$$

which is then reduced through reaction 4

$$CuCl_{ads} + e^- = Cu + Cl^- \qquad E^0 = -0.063 \text{ V}_{SCE} \qquad (4)$$

This chloride-mediated mechanism proceeds in parallel with the two-stage reduction of Cu^{2+} (reactions 1 and 2) and results in an acceleration of the overall reduction kinetics.[12]

The effect of chloride additions to the plating electrolyte on the morphology of electrodeposited copper has been investigated by Barkey et al.[13–15] Chloride was found to introduce anisotropy among the various crystallographic directions, favoring dendritic growth over tip splitting instabilities.[13] In addition, chloride ions were observed to stabilize terrace edges along the ⟨100⟩ directions and to favor a (001) orientation of copper films[15] In this article, we build on these findings and we study the correlation between the concentration of chloride in acidic sulfate electrolytes, the electrochemical kinetics of growth, and the phenomenon of dendrite formation, in particular their crystallographic orientation and morphology. We find that chlorides induce growth of dendrites only under growth conditions, which either approach diffusion limitations or occur at potentials where the various crystallographic surfaces exhibit a different potential dependence for chloride desorption. An additional, necessary condition for dendrite growth is that the Cu^+/Cu step (eq 4) becomes the rate-determining step in the system under study.

Experimental Section

All experiments were performed on As-doped, n$^+$-Si (100) wafers (Silicon Quest International, resistivity $\rho < 0.005 \ \Omega \cdot cm$) or polycrystalline copper (99.99%, oxygen free). The silicon samples were cleaned sequentially in methylene chloride, acetone, and ethanol for 20 min, respectively, then etched in 30% HF solution for 2 min to achieve hydrogen termination, and finally rinsed with Milli-Q water (resistivity $\rho > 18 \ M\Omega \cdot cm$). An ohmic contact was established at the backside of the substrate by applying an In−Ga eutectic alloy. Cu sheets were mechanically polished with silicon carbide paper up to 1200 grit, followed by electrochemical polishing in 85% phosphoric acid using a cell voltage of 1.7 V for 20 min, to achieve a mirror-like surface. The electrolytes for copper electrodeposition contained 10 mM (or 0.3 M) $CuSO_4$ + 0.5 M H_2SO_4 + x mM NaCl ($x = 0, 1, 4, 10, 100, 500$); pH was adjusted to 0.56 using NaOH. The solutions were prepared with analytical grade chemicals and Milli-Q water.

Electrochemical experiments were controlled and data recorded using an EG&G Princeton Applied Research potentiostat/
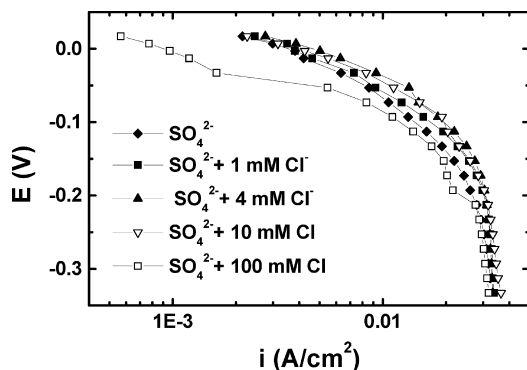
10098 *J. Phys. Chem. C, Vol. 113, No. 23, 2009*

Shao and Zangari

Figure 1. Steady-state current−potential curves at copper electrodes in 0.3 M CuSO$_4$ + 0.5 M H$_2$SO$_4$ with various concentrations of chloride (0−100 mM).

galvanostat (model 273A). The experiments and sample preparation were carried out in a three-electrode cell using a platinum mesh as the counter electrode and a Luggin capillary to separate the saturated calomel reference electrode (SCE) from the main compartment. The solutions were stirred and deaerated by nitrogen bubbling for 2 h before and during the experiment. All potentials are reported with respect to the SCE (0.242 V vs NHE). Steady-state current−voltage characteristics were obtained by applying a predetermined potential for at least 30 s or until the current was constant, before reading the corresponding current value. Cu films were grown on Si under potentiostatic control, carefully extracted from the electrolyte, rinsed with deionized water, dried in a nitrogen stream, and stored in a desiccator.

Field emission scanning electron microscopy (SEM, JEOL 6700F) was used to characterize the morphology of films onto n$^+$-Si (001). The crystallographic orientation of the dendrites in the deposits was analyzed by electron backscattering diffraction (EBSD) using a JEOL JSM 840 scanning electron microscope with a HKL Technology EBSD system. The Kikuchi patterns were automatically indexed, and the data obtained from EBSD were analyzed, using HKL Technology Channel 5 suite of programs.

Results

Cyclic voltammetry at both copper and silicon electrodes was used to study the effect of chloride addition and concentration on the electroreduction mechanism of copper from acidic sulfate solutions. The detailed analysis of these data was presented in ref.[16] In summary, it was found that the presence of chloride ions causes two competing effects: at low chloride concentration (a few millimoles per liter) the formation of an adsorbed chloride layer mediates copper reduction and introduces an additional reaction pathway, resulting in an overall depolarization of the reduction process; on the contrary, chloride polarizes copper deposition when its concentration is higher than 100 mM, due to the complexation of copper ions by chloride, which causes a net decrease in the concentration of free cupric ions.

Trends similar to those observed in the cyclic voltammograms are also seen in steady-state current−potential i−V curves obtained *at copper electrodes*,[16] as shown in Figure 1. Kinetic parameters of the Cu reduction reaction were quantified through a least-squares fitting of these curves, which was performed both using a Tafel approximation in the potential range from −0.10 to +0.02 V (Figure 2) and using a mass transport correction to the Tafel characteristics in the voltage range −0.15 to 0.02 V using the equation[17]

$$\eta = a + b \log \frac{(i_1 - i)}{i} \qquad (5)$$

where η is the overvoltage, i_1 is the limiting current density, a is a constant, and b is the Tafel slope. Experimental values for i_1, in the range 32−40 mA/cm^2 (Figure 1), were used in the fitting procedure. The two methods yield slightly different results. The resulting Tafel slopes (inset of Figure 2) are in the range 118−140 mV/decade (110−114 mV/decade with mass transport correction) in the solutions without or with chloride up to 10 mM, close to the reported value of 120−135 mV/decade.[18] This is consistent with copper reduction mainly occurring through two consecutive electron transfer steps (eqs 1 and 2), in which the first step is the RDS.[8−10] This mechanism appears little perturbed by the presence of adsorbed chloride ions. On the contrary, fitting the i−V curve for the solution containing 0.1 M NaCl yields a Tafel slope $b \sim 78$ mV/decade without and 79 mV/decade with mass transport correction, significantly smaller than the former values, but still higher than the value of 50−60 mV/decade measured in pure chloride solutions with higher concentration.[19] This suggests that the Cu reduction path through reactions 3 and 4 may become predominant in the solution with high chloride concentration. Additional evidence of this effect is the observation of a crossover behavior in the i−V curve around −0.04 V$_{SCE}$, clearly visible in Figure 1, which may be associated with the desorption of a chloride monolayer.

The theoretical Tafel slope for the chloride-mediated reaction mechanism described by eqs 3 and 4 can be calculated assuming reaction 4 to be the RDS. A value of 40 mV/decade was obtained, showing a large discrepancy between the experimental and theoretical values. This is probably due to the fact that even in pure chloride solutions the rate of copper reduction through reactions 1 and 2 cannot be entirely neglected. The coexistence of the two reaction paths 1 + 2 and 3 + 4 occurring at a similar rate would thus result in an i−V characteristics superposition of the i−V characteristics for the two paths, i.e., in an overall non-Tafel characteristics, that could be approximated by an effective Tafel slope always larger than that calculated for the chloride only route. The discrepancy observed between our results and those of ref 19 could thus be understood in view of the fact that the chloride concentration in the present experiments was lower. The slight decrease in Tafel slope with increasing Cl$^-$ concentration (Figure 2) could similarly be understood as a consequence of an increasing influence of the chloride mediated route.

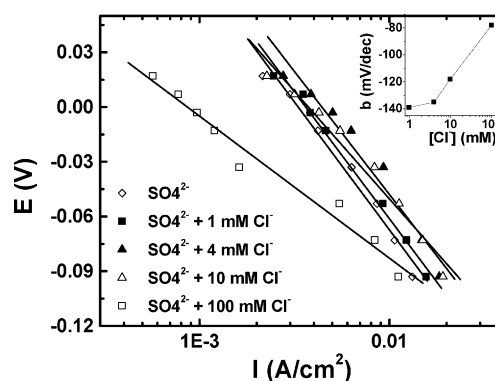Cu films were grown to an equivalent thickness of about 480 nm by potentiostatic deposition at −0.55 V$_{SCE}$ *on n$^+$-silicon*

Figure 2. Tafel plots for copper deposition in 0.3 M CuSO$_4$ + 0.5 M H$_2$SO$_4$ with various concentrations of chloride (0−100 mM). Inset: fitted Tafel slope vs Cl$^-$ concentration.

Dendritic Growth in Copper Electrodeposition

J. Phys. Chem. C, Vol. 113, No. 23, 2009 **10099**

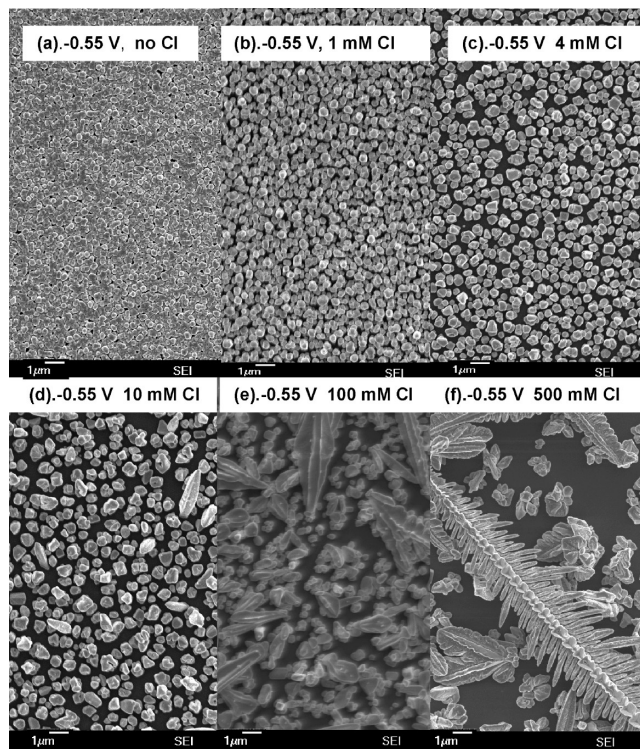**Figure 3.** (a−f) Copper deposits obtained at −0.55 V on hydrogen-terminated silicon from 10 M $CuSO_4$ + 0.5 M H_2SO_4 with various chloride concentrations. The charge deposited was 0.8 C/cm^2 (1333 monolayers, ~480 nm).

Figure 4. SEM image of a copper film deposited onto silicon in a 10 mM $CuSO_4$ + 0.5 M H_2SO_4 with 0.5 M NaCl electrolyte. The film was deposited using a nucleation pulse of −0.65 V_{SCE} for 1 s, followed by growth at −0.40 V_{SCE}. The charge deposited was 0.8 C/cm^2 (1333 monolayers).

Figure 5. SEM image of a dendritic deposit obtained in 10 mM $CuSO_4$ + 0.5 M H_2SO_4 with 0.5 M NaCl and the corresponding $\langle 110 \rangle$ pole figure. The charge deposited was 0.8 C/cm^2 (1333 monolayers). X1, Y1 is the coordinate system of data acquisition in the EBSD system; the axes are on the sample surface. The $\langle 110 \rangle$ pole figure below demonstrates that the direction of the main branch corresponds with one of the $\langle 110 \rangle$ directions.

substrates, using a Cu^{2+} concentration of 10 mM to limit the growth kinetics. SEM images of the resulting films are shown in Figure 3. Three-dimensional Volmer−Weber type growth was observed, with the number density of nuclei decreasing and the average nucleus size increasing with increasing chloride concentration. Only the deposits in chloride-free solution appear to form a continuous Cu film. Higher [Cl$^-$] concentration also yields nuclei with increased faceting. Deposition from a 10 mM NaCl solution results in the formation of some needle-like crystals; their concentration strongly increases upon a 10-fold increase of the NaCl concentration. Dendritic crystals with well-developed side branches are present when growing from a 500 mM chloride solution. The angles between the main and the side branches of these dendrites are all about 60°, suggesting a well-defined correlation between the crystallographic directions of the side branches. Films of the same average thickness obtained by an initial nucleation pulse at −0.65 V for 1 s, followed by growth at −0.4 V_{SCE}, on the contrary exhibit grain faceting but no dendrite formation, as shown in Figure 4.

EBSD was carried out to determine the orientation of the main and side branches of the dendrite shown in Figure 5. The regions marked "1" and "2" on the main branch exhibit the same Kikuchi pattern, which is also identical to the patterns obtained from the regions marked "3" and "4" on the side branches, as shown in Figure 6. This indicates that all these regions have equivalent crystallographic orientations. The pole figures of grain "1" along various crystallographic directions of low Miller indices were constructed from the Kikuchi pattern and are shown in Figure 7. A 6-fold symmetry, corresponding to a 60° angle between equivalent directions, is found only in the $\langle 110 \rangle$ and $\langle 211 \rangle$ pole figures, as can be observed from the three points on the left upper edges of the corresponding projection circles (the other three points are not observed due to the slight tilt of the dendrite). Comparing the direction
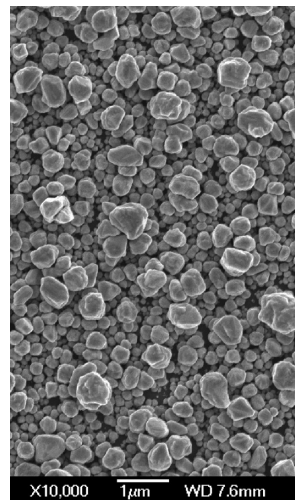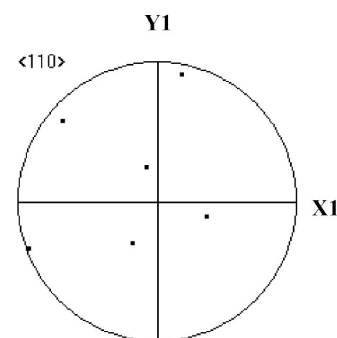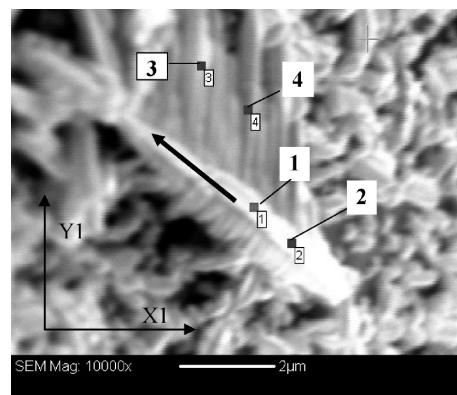
(marked with an arrow) of the main branch of the dendrite shown in Figure 5 with the structure of the $\langle 110 \rangle$ and $\langle 211 \rangle$ pole figures, it can be concluded that the main branch of the dendrite grows along the $\langle 110 \rangle$ direction. In fact, the direction of the main branch coincides with one of the $\langle 110 \rangle$ directions, as clearly shown by the comparison of the directions of the main and side branches of the dendrite with the $\langle 110 \rangle$ pole figure in Figure 5, but with none of the $\langle 211 \rangle$ directions.

Figure 6. EBSD Kikuchi pattern of the dendrite shown in Figure 5.

The ⟨100⟩, ⟨110⟩, and ⟨111⟩ pole figures of all four regions highlighted in Figure 5 are shown in Figure 8. The pole figures coincide, further confirming equivalent crystallographic orientations; in addition, the three ⟨110⟩ directions coincide with the directions of the main and side branches of the dendrite in Figure 5. It also can be seen from the ⟨111⟩ pole figure that the (111) plane of all grains is almost parallel to the sample surface; in fact, one of the reflections is present at the center of the projection circle. Because of this crystal orientation and the symmetry of the face-centered cubic system, the orientation of the grains remains invariant upon 120° rotation around the direction perpendicular to the sample surface, explaining why the grains on both main and side branches show the same Kikuchi pattern. The inverse pole figures for all regions "1"−"4" along the X1 direction as shown in Figure 5 are displayed in Figure 9a, confirming that all regions have the same crystallographic orientation along X1. X1 however is not along ⟨110⟩, since this direction is neither the direction of the main branch nor of any side branch. The inverse pole figures along the direction of the main branch were thus redrawn by rotating X1 counterclockwise by 136.82°, as calculated from the coordinates of grain "1" and "2"; the result is shown in Figure 9b. Now all grains exhibit a ⟨110⟩ orientation along this direction, further proving that the dendrite indeed grows along the ⟨110⟩ direction.

The SEM image of Figure 10 details the morphology of the main branch of a typical dendrite. Truncated arms are observed to grow off the main branch, with (111) triangular facets perpendicular to the substrate surface, and {311} facets adjacent to the former. Side branches shoot out of the main branch, growing along the [110] and [$\bar{1}$10] directions.

Discussion

Growth morphology is determined jointly by ion diffusion toward the growth front and interface parameters such as interface tension and interface kinetics. In particular, anisotropy in the interface properties is a necessary condition to observe dendritic growth; without anisotropy only fractal diffusion limited aggregation or tip-splitting morphologies can be obtained.[1] It is difficult to assess with certainty whether growth in our experimental conditions occurs under diffusion limitations. Steady-state $i-V$ curves for the 10 mM Cu^{2+} solution of copper substrates give a limiting current density of 1.1−1.2 mA/cm². Growth at −0.55 V_{SCE} on silicon occurs at an average current density of 0.43 (no Cl^-) and 0.27 (500 mM Cl^-) mA/cm², well below the limiting current density. These values however are not representative of the actual current densities at the growth sites, which are likely much higher in the high chloride solutions, due to the growth front being limited at the dendrite tips. Our observation that no dendrites are observed when growing at −0.4 V_{SCE} however supports the hypothesis that growth at −0.55 V_{SCE} in the high chloride solution occurs

under at least partial diffusion limitations. Another possibility is that the different potential dependence of the disordering/desorption process of the Cl adlayer on surfaces with different crystallographic orientation could also result in such potential dependence of the morphology. The experiments reported here are unable to distinguish between these two possibilities. In the framework of the former explanation, the fact that neither dendrites nor tip splitting are observed in the sulfate solution at the same potential is likely due to the fact that the density of growth sites is much larger and the current density consequently lower than the limiting current density.

Disordered (tip-splitting) growth patterns have been observed under diffusion limitations in the absence of pronounced anisotropy, as exemplified in a number of electrochemical deposition experiments.[13,14,20,21] Anisotropy on the other hand is required to stabilize needle-like and dendritic growth.[22] The presence of chloride anions has been observed to induce anisotropy in Cu electrodeposition, sufficient to observe a transition from tip splitting to dendritic growth.[13] However, morphology of Cu electrodeposits has also been found to depend on applied potential, with dendritic growth achievable in absence of chloride at sufficiently high overvoltage.[14]

We argue that chloride introduces indeed anisotropy in growth velocity due to differences in the extent of chloride adsorption on the various crystallographic faces and that this anisotropy results in the formation of dendrites when growth occurs near to the diffusion limit or at potential values within the range where chloride desorption from different crystallographic surfaces exhibit different potential dependence. An additional necessary condition is that the anisotropic interface process should be the rate-limiting process.

Chloride adsorption on single crystal copper surfaces has been extensively studied in perchloric acid with addition of chloride or pure chloride solutions, as summarized for example in ref 23. For the Cu(100) surface, in situ STM by Suggs and Bard[24] and Moffat[25] indicate the formation of a $(\sqrt{2} \times \sqrt{2})R$ 45° (equivalent to the c(2 × 2)) chloride adlayer structure in the potential region where no substrate dissolution occurs. The in situ STM study by Vogt et al.[26] shows a c(2 × 2) chloride adlayer on Cu(100) only at potentials above −400 mV vs Ag/AgCl. The in situ video STM by Magnussen et al.[27] also revealed a c(2 × 2) chloride adlayer on Cu(100). The coverage of chloride corresponding to all these structures has the same value of 0.50. For the Cu(111) surface, the in situ STM study by Suggs and Bard[28] shows a $(6\sqrt{3} \times 6\sqrt{3})R$ 30° chloride adlayer over the entire investigated potential range. Moffat also found such an incommensurate chloride adsorption structure on Cu(111).[25] The in situ STM studies on Cu(111) by Kruft et al.[29] and Broekmann et al.[30] show a different $((\sqrt{3} \times \sqrt{3})R$ 30° chloride adlayer structure. The in situ STM and LEED in ultrahigh vacuum studies by Itaya et al. show a different c($p \times \sqrt{3}$ R30°) (p = 2.53−2.48) chloride adlayer structure on Cu(111).[31] The chloride coverage corresponding to these structures is 0.45, 0.33, and 0.395−0.403, respectively. For the Cu(110) surface, in situ STM by Itaya[32] reveals a (4 × 1) chloride adlayer structure on the reconstructed Cu surface. The in situ STM by Li et al.[33] shows that there exist two chloride adlayer structures on the Cu(110) reconstructed surface: a (4 × 1)structure containing three chloride anions per unit cell and a (5 × 1)structure containing four chlorides. The chloride coverage corresponding to these structures is 0.75, 0.75, and 0.80, respectively. Clearly, the chloride coverage is highest on Cu(110), most probably due to its most open structure.[33]
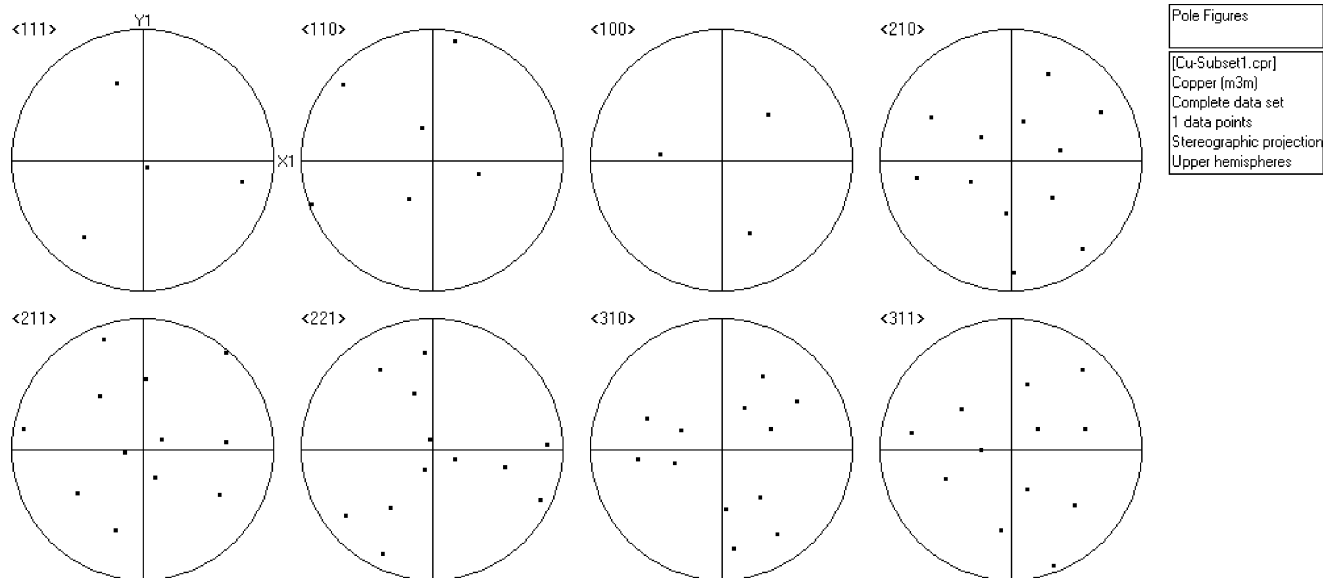
Figure 7. The ⟨100⟩, ⟨110⟩, ⟨111⟩, ⟨210⟩, ⟨211⟩, ⟨221⟩, ⟨310⟩, ⟨311⟩ pole figures of the region marked with "1" in Figure 5. X1, Y1 is the coordinate system of acquisition surface in the EBSD system; the axes are in the sample surface. Z points outward at the center of pole figures.
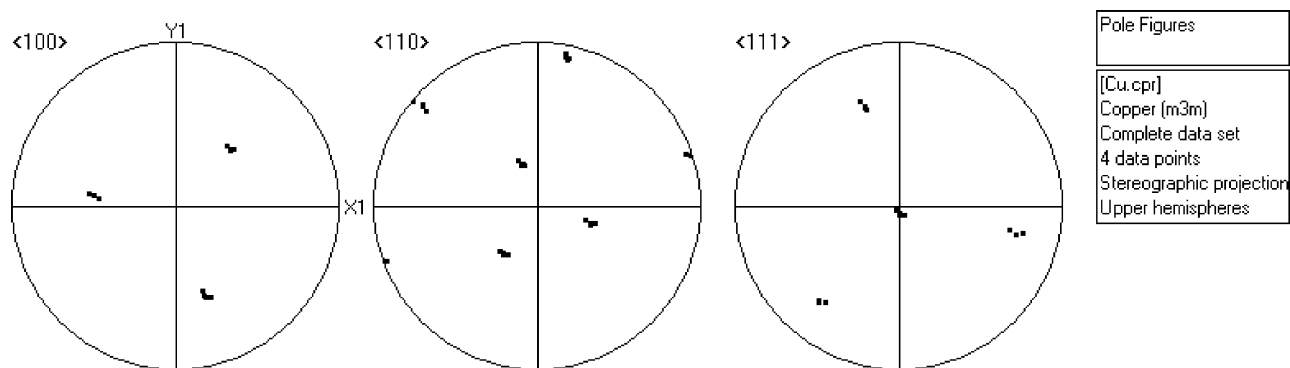

Figure 8. The ⟨100⟩, ⟨110⟩, and ⟨111⟩ pole figures of the four regions marked with "1", "2", "3", and "4" in Figure 5.
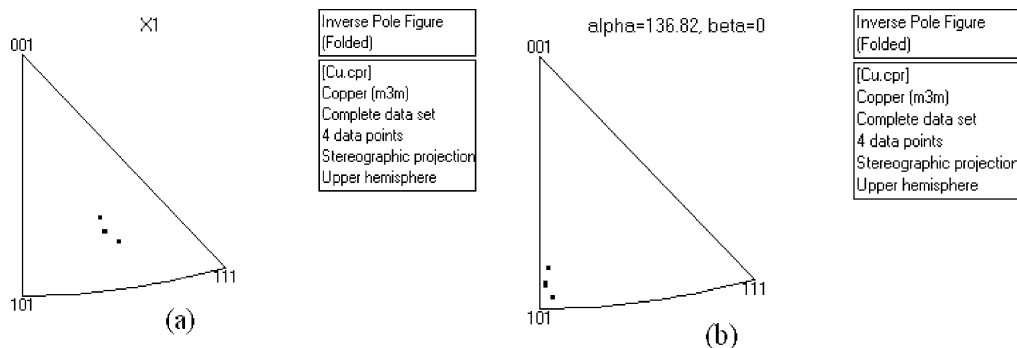

Figure 9. The inverse pole figure (a) along X1 and (b) along the main branch direction of the dendrite shown in Figure 5.

Chloride anions on the copper surface accelerate the Cu reduction reaction. Such catalytic effects can be seen either as a consequence of the introduction of an additional reaction route (eq 3 followed by eq 4) or as a decrease in the energy barrier of reaction 1 due to bridging chloride anions.[12] A higher chloride coverage on {110} surfaces would increase the growth rate in the perpendicular directions ⟨110⟩, eventually resulting in an instability and in the formation of dendrites with the same preferential orientation.

Such mechanism however determines the final morphology only when the chloride-mediated reduction path is rate-determining. Thus, while chloride adlayer structures on Cu can be formed even with very small chloride concentrations in solution,[23−33] large chloride concentrations are required for the chloride route to become rate determining, as shown by the variation of Tafel slope vs chloride concentration (Figure 2). Correspondingly, chloride concentrations larger than 100 mM are required to observe well-developed dendrites, but 10 mM concentration may be sufficient to induce the growth of needle-like structures (Figure 3), which may still be harmful in applications.

Conclusions

The morphology of Cu films electrodeposited onto Si from an acidic sulfate electrolyte with the addition of chloride anions
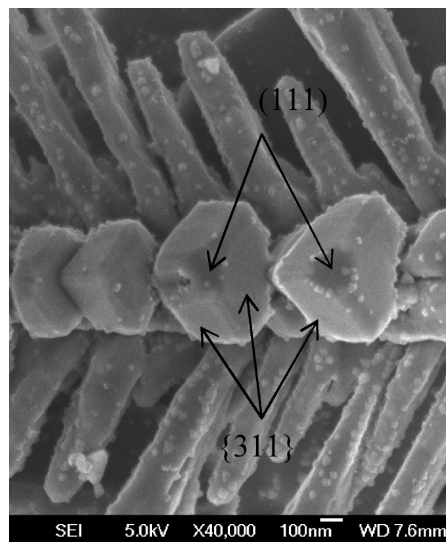
Figure 10. The SEM image (tilted 8°) at high magnification of a dendrite in the sample deposited at −0.55 V. The charge deposited was 0.8 C/cm² (1333 monolayers).

in the range 1−500 mM was investigated. While in sulfate solutions small, nonfaceted grains are observed, addition of chloride increases grain size and the degree of grain faceting, while decreasing nucleus density. Needle-like structures are observed for $[Cl^-] \geq 10$ mM and well-developed monocrystalline dendrites are observed for $[Cl^-] = 500$ mM. Dendrites develop under growth conditions that either approach diffusion limitations or occur at potential values within the range where different crystallographic surfaces exhibit a different potential dependence for chloride adlayer desorption. In any case, dendrite formation is mainly due to the introduction of anisotropy at the interface, which stabilizes dendritic growth when the chloride reduction route $Cu^{2+} \rightarrow CuCl \rightarrow Cu$ is the rate-determining step. A probable reason for dendrite growth occurring along the $\langle 110 \rangle$ directions is that the $\{110\}$ planes are characterized by the largest chloride adsorption and their growth rate is consequently the highest.

References and Notes

(1) Ben-Jacob, E.; Garik, P. *Nature* **1990**, *343*, 523.
(2) Barkey, D. P. Structure and pattern formation in electrodeposition. In *Advances in Electrochemical Science and Engineering,* Vol. 7, Alkire, R. C., Kolb, D. M., Eds.; Wiley: New York, 2001; p 151.
(3) Andricacos, P. C.; Uzoh, C.; Dukovic, J. O.; Horkans, J.; Deligianni, H. *IBM J. Res. Dev.* **1998**, *42*, 567.
(4) Reid, J. D. *Jpn. J. Appl. Phys* **2001**, *40*, 2650.
(5) Cooper, E. I.; Bonhote, C.; Heidmann, J.; Hsu, Y.; Kern, P.; Lam, J. W.; Ramasubramanian, M.; Robertson, N.; Romankiw, L. T.; Xu, H. *IBM J. Res. Dev.* **2005**, *49*, 103.
(6) Andricacos, P. C.; Robertson, N. *IBM J. Res. Dev.* **1998**, *42*, 671.
(7) Shin, H. C.; Dong, J.; Liu, M. *Adv. Mater.* **2003**, *15*, 1610.
(8) Bockris, J.; O', M.; Mattson, E. *Trans. Faraday Soc* **1959**, *55*, 1586.
(9) Bockris, J.; O', M.; Enyo, M. *Trans. Faraday Soc* **1962**, *58*, 1187.
(10) Brown, O. R.; Thirsk, H. R. *Electrochim. Acta* **1965**, *10*, 383.
(11) Soares, D. M.; Wasle, S.; Weil, K. G.; Doblhofer, K. *J. Electroanal. Chem.* **2002**, *532*, 353.
(12) Nagy, Z.; Blaudeau, J. B.; Hung, N. C.; Curtiss, L. A.; Zurawski, D. J. *J. Electrochem. Soc.* **1995**, *142*, L87.
(13) Barkey, D.; Oberholtzer, F.; Wu, Q. *Phys. Rev. Lett.* **1995**, *75*, 2980.
(14) Oberholtzer, F.; Barkey, D.; Wu, Q. *Phys. Rev. E* **1998**, *57*, 6955.
(15) Wu, Q.; Barkey, D. *J. Electrochem. Soc.* **2000**, *147*, 1038.
(16) Shao, W.; Pattanaik, G.; Zangari, G. *J. Electrochem. Soc.* **2007**, *154*, D201.
(17) Bard, A J.; Faulkner, L. R. *Electrochemical Methods: Fundamentals and Applications*; John Wiley & Sons: New York, 1980.
(18) Doblhofer, K.; Wasle, S.; Soares, D. M.; Weil, K. G.; Weinberg, G.; Ertl, G. *Z.Phys. Chem.* **2003**, *217*, 479.
(19) Astakhova, R. K.; Krasilov, B. S. *Zh. Prikl. Khim* **1971**, *44*, 363. Cited in*Encyclopedia of Electrochemistry of the elements, Vol. II, Chapter II-6*; Bard, A. J.; Ed.; Marcel Dekker, Inc.: New York, 1974; p 438.
(20) Sawada, Y.; Dougherty, A.; Gollub, J. P. *Phys. Rev. Lett.* **1986**, *56*, 1260.
(21) Grier, D.; Ben-Jacob, E.; Roy, Clarke; Sander, L. M. *Phys. Rev. Lett.* **1986**, *56*, 1264.
(22) Ben-Jacob, E.; Goldenfeld, N.; Langer, J. S.; Gerd Schön, *Phys. Rev. Lett.* **1983**, *51*, 1930.
(23) Magnussen, O. M. *Chem. Rev.* **2002**, *102*, 679.
(24) Suggs, D. W.; Bard, A. J. *J. Phys. Chem.* **1995**, *99*, 8349.
(25) Moffat, T. P. *Mat. Res. Soc. Sym. Proc.* **1997**, *45*, 75.
(26) Vogt, M. R.; Lachenwitzer, A.; Magnussen, O. M.; Behm, R. *J. Surf. Sci.* **1998**, *399*, 49.
(27) Polewska, W.; Behm, R. J.; Maggnussen, O. M. *Electrochim. Acta* **2003**, *48*, 2915.
(28) Suggs, D. W.; Bard, A. J. *J. Am. Chem. Soc.* **1997**, *116*, 10725.
(29) Kruft, M.; Wohlmann, B.; Stuhlmann, C.; Wandelt, K. *Surf. Sci.* **1997**, *377*, 601.
(30) Broekmann, P.; Wilms, M.; Kruft, M.; Stuhlmann, C.; Wandelt, K. *J. Electroanal. Chem.* **1999**, *467*, 307.
(31) Inukai, J.; Osawa, Y.; Itaya, K. *J. Phys. Chem. B* **1998**, *102*, 10034.
(32) Wan, L.-J.; Itaya, K. *J. Electroanal. Chem.* **1999**, *473*, 10.
(33) Li, W. H.; Wang, Y.; Ye, J. H.; Li, S. F. Y. *J. Phys. Chem. B* **2001**, *105*, 1829.

JP8095456